



Cite this: *Soft Matter*, 2016, 12, 9246

The effect of confinement on the electrohydrodynamic behavior of droplets in a microfluidic oil-in-oil emulsion†

Somayah Khajepour Tadavani,* James R. Munroe and Anand Yethiraj*

A two-fluid emulsion (silicone oil drops in the “leaky dielectric”, castor oil) with electrohydrodynamically driven flows can serve as a model system for tunable studies of hydrodynamic interactions [Varshney *et al.*, *Sci. Rep.*, 2012, **2**, 738]. Flows on multiple length- and time-scales have been observed but the underlying mechanism for these chaotic, multi-scale flows is not understood. In this work, we conducted experiments varying the thickness of the test cell to examine the role of substrate interactions on size distribution, mean square displacement and velocity of the drops as a function of the electric field strength. We find that the electric capillary number, Ca_E , at the threshold of drop breakup is of order unity for cell thicknesses of 100 μm or thicker, but much larger for thinner cells. Above this threshold, there is a clear transition to super-diffusive droplet motions. In addition, we observe that there is a convective instability prior to the onset of chaotic flows, with the lengthscale associated with the convection rolls increasing linearly with an increase in the cell thickness. The fact that the convective instability appears to occur in the leaky dielectric castor oil regardless of whether the second component is liquid drops, solid particles, or dissolved dye has implications on the underlying mechanism for the unsteady flows.

Received 19th July 2016,
Accepted 21st October 2016

DOI: 10.1039/c6sm01648k

www.rsc.org/softmatter

1 Introduction

Several experimental model systems have realized tunable near-equilibrium self-assemblies,^{1–3} but there are fewer good model systems for far-from-equilibrium self-assemblies.⁴ Electrohydrodynamics – fluid motion induced by electric fields –⁵ provides a tuning parameter to drive an otherwise dissipative, low-Reynolds number fluid out of equilibrium. Liquid drops exposed to an external electric field and surrounded by another liquid respond in a variety of ways. They can deform, rotate, coalesce, or break up.⁶ The coupling between fluid motion and the electric field is used for a wide range of applications; two examples are electrohydrodynamic pumps⁷ and ink-jet printing.⁸

Drop deformation has been extensively studied theoretically and experimentally during the past six decades.^{9–15} The theoretical description of immiscible drop behavior in a second liquid and in an electric field typically invokes the “leaky dielectric model”.¹² The model relates the accumulation of free charges at the liquid–liquid interface to a tangential component of the electric stress (which gives rise to electrohydrodynamic forces),

which in turn competes with the normal electrostatic stress (*i.e.* dipolar forces) at the interface. Depending on the angular variation of stresses, or the strength of the applied electric field, the drop gives rise to shape deformation, or breakup.^{12–14}

This study focuses on the collective behavior within a test cell of many silicone oil drops in a medium of castor oil, interacting *via* long-range electrohydrodynamic forces. The strength of the hydrodynamic interactions are modulated by changing the amplitude of a DC electric field. In this system, violent breakup of silicone oil drops has been observed¹⁶ above a threshold value of the electric field, followed by multi-scale flows that exhibit scale invariance in the intensity and stress fluctuations.¹⁷ The flows in this “strong hydrodynamic” regime – *i.e.* hydrodynamic forces dominating over dipolar forces – are reminiscent of turbulent behaviour. Turbulence in fluid mechanics is often associated with high Reynolds number Re , but in this system $Re < 10^{-5}$. Low Reynolds number turbulence, at Re ranging from 10^{-5} – 10^{-1} , has indeed been observed and studied in visco-elastic polymer solutions,¹⁸ and in electrokinetically forced pressure-driven flow in microchannels.¹⁹ In the present experimental system, however, the underlying mechanisms for the multi-scale flow remains unclear. While the leaky dielectric model provides useful insights, it is likely to break down where the Debye screening length, κ^{-1} , is of order the droplet size, a ; this is the case in the

Physics and Physical Oceanography, Memorial University of Newfoundland, St. John's, NL, A1B 3X7, Canada. E-mail: skt660@mun.ca, ayethiraj@mun.ca

† Electronic supplementary information (ESI) available. See DOI: 10.1039/c6sm01648k

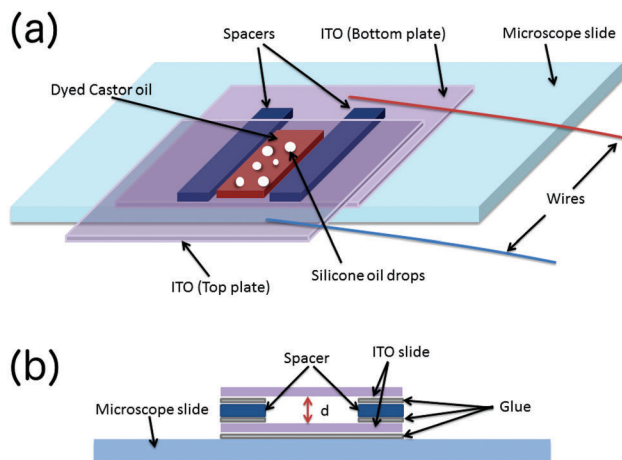


Fig. 1 A schematic design of the microfluidic cell geometry: (a) perspective and (b) side view. Electric field is perpendicular to the substrate and parallel to gravity.

current study. Studies that account for electrokinetic transport near the droplet interface^{20,21} have thus far either considered $\kappa^{-1} \ll a$ (and large external fields), or the limit of small deformations for a range of κ^{-1} .

A key question relates to what role the dimensionality of the sample, or confinement by the bounding substrates, plays. This question is relevant because the sample cell (see Fig. 1 and description in the Methods and techniques section) is much thinner in the vertical dimension (a few hundred micrometers) than in its lateral extent (centimeters). The bounding plates in the vertical dimension are conducting substrates, which are also the electrodes. It is thus unclear if this microfluidic system is effectively two-dimensional or three-dimensional. To address this question, we vary the cell thickness, d , in order to examine the substrate–droplet interactions and the differences between quasi-two dimensional systems and three dimensional ones. As a function of cell thickness, and at different electric fields, we examine droplet size distributions, mean-squared displacement of the drops *versus* time, and droplet velocities.

2 Methods and techniques

Fig. 1 shows a schematic design of a test cell with the electric field perpendicular to the microscope slide and parallel to gravity. Two indium tin oxide (ITO) coated cover glass slides are separated by glass or plastic spacers with defined thicknesses. The plates and spacers are held together with ultraviolet-curable epoxy (Norland Optical Adhesive 61 and 68). The ITO slides are optically transparent and electrically conductive, which enables their use both as electrodes and to image through them as with regular glass. The cell is filled by pipetting an emulsion of silicone oil (dielectric constant $\epsilon_{in}/\epsilon_0 = 2.4$, conductivity $\sigma_{in} = 3.95 \times 10^{-11} \text{ S m}^{-1}$, and viscosity $\mu_{in} = 0.137 \text{ Pa s}$) and castor oil (dielectric constant $\epsilon_{ex}/\epsilon_0 = 3.6$, conductivity $\sigma_{ex} = 4.0 \times 10^{-10} \text{ S m}^{-1}$, and viscosity $\mu_{ex} = 0.819 \text{ Pa s}$). The subscripts *in* and *ex* are used to represent the droplet

and the suspending fluid, respectively. The emulsion was prepared first by mixing silicone oil and castor oil in a volume ratio of 1:16. Then, it was vortexed by a vortex mixer for 5 minutes. This leads to a uniform dispersion of tiny silicone oil drops, with different sizes, in the castor oil. The cell was immediately filled after preparing the emulsion.

The lateral dimension of cells is between 0.5 and 1 cm, while the vertical dimension, or the cell thickness, d , varies as 27, 55, 96, or 202 μm . The strength of the DC electric field is varied from 0 up to $18 \text{ V } \mu\text{m}^{-1}$ in intervals of $1 \text{ V } \mu\text{m}^{-1}$.

The conductivity and the dielectric constant of oils were measured by impedance spectroscopy using an impedance analyzer, a potentiostat/galvanostat (Princeton Applied Research model 273A) attached to a lock-in amplifier (Signal Recovery model 5210), in the 0.1 Hz to 100 kHz frequency range. The frequency dependence, $|Z| = R/(1 + (fRC)^2)^{1/2}$, was fitted and R and C were obtained. The conductivity, $\sigma = d/RA$, and the dielectric constant, $\epsilon = \epsilon_0 A/Cd$, where d , A , ϵ_0 are the gap distance between the two parallel plates, cell area, and permittivity of vacuum, respectively, were then calculated from R and C .

After recording an experiment with a water-cooled digital sCMOS camera (pco.edge 5.5), the shapes and positions of the droplets are found. An edge finding algorithm, written in the image processing software, Fiji (<http://fiji.sc/Fiji>), is used to find the edge of the drops based on the gradient of image intensity as the edge finding method. For every frame in a video sequence, or stack, the centroid, (x, y) , and area of every drop is measured. After identifying the coordinates of the droplets one is able to track their motion using particle tracking. This is done using code described by Crocker and Grier.²²

From this, we obtain the mean square displacement, $\text{MSD} \equiv \langle r^2 \rangle$, where r is the magnitude of the displacement of each drop as a function of the time t (from a reference start time t_0), and $\langle \cdot \rangle$ is an average over all the drops in the system, and over the reference time. One can write $\text{MSD} \sim t^\gamma$, where $\gamma = 1$ for diffusive motion, and is larger for advection and smaller for constrained diffusion.

For particle imaging velocimetry (PIV) an open source implementation, *CivX*, is used.^{23,24} Interrogation windows with a size that is roughly twice the drop diameter are used and the displacement is estimated from cross-correlation of consecutive frames. Here, we are using PIV as a form of interfacial velocimetry (the analog of the “tracer particles” are the points on the drop interface).

We also carry out experiments with fluorescent PMMA colloids (diameter of $1 \mu\text{m}$) suspended in castor oil and in a volume ratio of 1:80. The PMMA particles are charged, and when the sign of the electric field is switched, particles migrate from the positive to the negative electrode with a speed proportional to the electric field ($7 \mu\text{m s}^{-1}$ for $E = 1 \text{ V } \mu\text{m}^{-1}$, yielding an electrophoretic mobility $M \sim 7 \mu\text{m}^2 \text{ V}^{-1} \text{ s}^{-1}$). We also carried out experiments on the diffusion of the dye (Nile red) in castor oil, using white light illumination and time-lapse macro scale photography. These results are presented in Section 3.5.

3 Results and discussion

3.1 Breakup and coalescence of drops

The droplet breakup mechanism is studied as a function of the cell thickness, d , and amplitude of the DC electric field, E . We begin with the thinnest cell ($d = 27 \mu\text{m}$). Upon increasing the electric field, one observes, at a threshold field of $8.5 \text{ V } \mu\text{m}^{-1}$, that large drops, with lateral (cross-section) radius roughly between 80 and $180 \mu\text{m}$ (*i.e.* much wider than the cell thickness), break up into smaller ones. Fig. 2(a) shows the breakup of one such large drop at $E = 9.5 \text{ V } \mu\text{m}^{-1}$. The bottom of the drop is in complete contact with the substrate while most of the

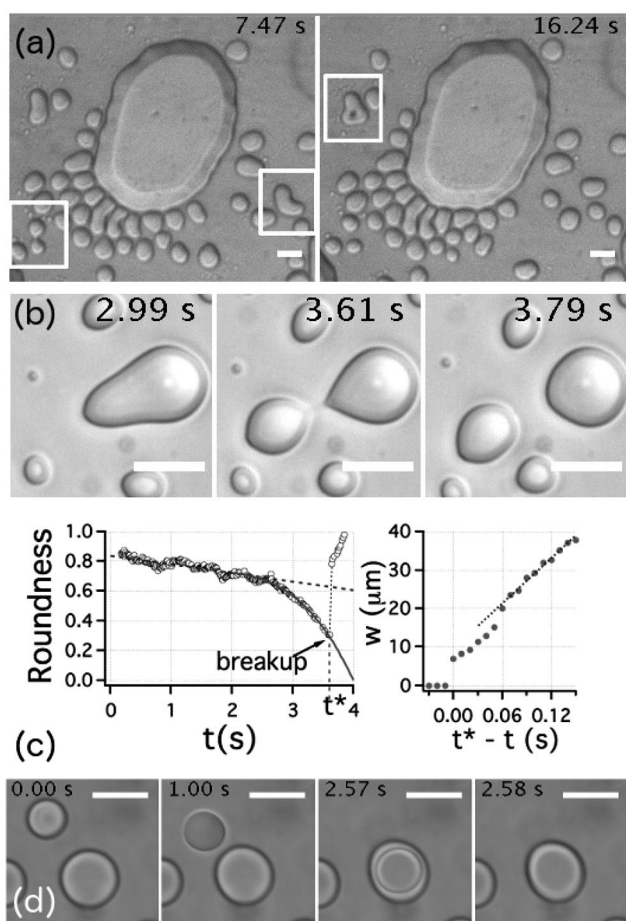


Fig. 2 Drop breakup and coalescence in a DC electric field. (a) $d = 27 \mu\text{m}$. The edge of a big drop fluctuates with a wavelength of roughly $40 \mu\text{m}$ and drops of comparable diameter are generated from these fluctuations. The white boxes highlight regions where drop breakup is occurring. $E = 9.5 \text{ V } \mu\text{m}^{-1}$. (b) $d = 55 \mu\text{m}$. Droplet breakup phenomenon for oblate spheroidal deformations occurs with drop being pulled apart laterally, perpendicular to the electric forcing. (c) The breakup is slow with a linear decrease in roundness for 2 seconds, prior to a more rapid decrease until breakup occurs (at $t = t^* = 3.61 \text{ s}$); the latter is accompanied by a decrease in the width w of the neck: just prior to breakup the neck is $7 \mu\text{m}$ wide. (b and c) $E = 8.5 \text{ V } \mu\text{m}^{-1}$. (d) $d = 96 \mu\text{m}$. Coalescence of two deformed (oblate spheroidal) droplets. Drop coalescence is achieved by the self-alignment and attraction along the DC electric field; the cell is now thick enough to accommodate two drops atop each other. $E = 3.5 \text{ V } \mu\text{m}^{-1}$. In all figures, the electric field is perpendicular to the page, and the scale bar is $50 \mu\text{m}$.

top is in contact with the top electrode, except for a meniscus which is roughly $50 \mu\text{m}$ wide. As the magnitude of the electric field increases, the edge of the drops fluctuate and create a natural wavelength ($\approx 40 \pm 9 \mu\text{m}$), and droplets are generated with diameter that are all comparable or slightly larger than the natural wavelength and roughly twice the cell thickness of $d = 27 \mu\text{m}$. The white rectangles highlight the three breakup events that occur in the region of interest over several seconds. This may be seen in Movie S1 (left panel) (ESI†).

For a cell that is roughly twice as thick ($d = 55 \mu\text{m}$), shown in Fig. 2(b), drop deformation is observed first for the largest drops (with initial cross-section radius roughly between 20 and $115 \mu\text{m}$) at $E = 4.5 \text{ V } \mu\text{m}^{-1}$. At $6.5 \text{ V } \mu\text{m}^{-1}$, the edge deformations gives rise to droplet breakup and smaller droplets are generated from the bigger ones. At this threshold field, the interfacial tension is overcome by the electric stress at the interface.

The breakup of one such drop, at $E = 8.5 \text{ V } \mu\text{m}^{-1}$, shown in Fig. 2(b) obtained at 100 frames per second for the complete time evolution, can be tracked as a function of time by any measure of the curvature: we use the “roundness”, defined as $4 \times \text{area}/(\pi D_{\text{major-axis}}^2)$. Fig. 2(c), (left) shows that the roundness as a function of time decreases linearly for more than 2 seconds before there is a sharper decrease (fitted to a power law) that coincides with the formation of a thin “neck” that eventually breaks. Fig. 2(c), (right) shows the width of this neck, w , which decreases rapidly over the fractions of a second prior to breakup, from $40 \mu\text{m}$ to about $7 \mu\text{m}$. This dynamics may be seen in Movie S1 (middle panel) (ESI†). What we are observing is crossover between two regimes of thinning: this has previously been observed in the thinning dynamics of liquid drops before breakup.²⁵

A third cell, again roughly twice as thick as the previous one, was made with a thickness of $d = 96 \mu\text{m}$. The initial cross section radius of drops varied from 9 to $282 \mu\text{m}$. The breakup phenomenon in this case began at $3.5 \text{ V } \mu\text{m}^{-1}$. A notable qualitative difference at this thickness is the much higher frequency of coalescence events. While for the thinnest cell ($d = 27 \mu\text{m}$) no coalescence of drops was observed even at high fields ($18.5 \text{ V } \mu\text{m}^{-1}$), coalescence was readily observed here. An example is seen in Fig. 2(d): at $t = 0 \text{ s}$, a drop detaches from the substrate, and approaches a second drop, riding on top of it so their flattest faces are in contact. This may also be seen in Movie S1 (right panel) (ESI†). This is clearly easier to achieve in a thicker cell, and thus coalescence is seen at the modest fields that drive drops into motion.

For the last and thickest cell, $d = 202 \mu\text{m}$, the initial cross sectional radii are between 17 and $244 \mu\text{m}$. The coalescence and breakup of drops start at low field, somewhere between $E = 1.5 \text{ V } \mu\text{m}^{-1}$ and $E = 2.5 \text{ V } \mu\text{m}^{-1}$ and the cell is thick enough to let drops move freely vertically. Although three-dimensional motion also happens in the third cell, it is more dominant and frequent in this thicker fourth cell.

Given the importance of the bounding surfaces, it is of interest to know if the contact angle changes with electric field. The contact angle of a silicone oil drop on glass, and in a castor oil environment, is measured (using a field geometry where the viewing direction is perpendicular to the field) to be $125 \pm 1^\circ$.

There is only a 2° difference between zero and high fields; therefore, given the uncertainties, we may say that there was no discernible change in contact angle with field strength.

Steady equilibrium deformation of a drop no longer exists if the electric field strength exceeds a critical value. The reported dynamics is either a tip-streaming deformation when $\epsilon_{\text{in}}/\epsilon_{\text{ex}} > 1$,^{26–29} or a pinch-off deformation which produces a bulbous-ended deformation and breakup when $\epsilon_{\text{in}}/\epsilon_{\text{ex}} < 1$.^{26,28,29} Fig. 2(b) shows a pinch off breakup with the electric field perpendicular to the thin thread. A new kind of deformation, a hole in the middle of a bigger drop, prior to the breakup event was also seen at $d = 27 \mu\text{m}$, Fig. 2(a).

3.2 Droplet size statistics in thin and thick cells

Next, we examine the drop size statistics, as a function of cell thickness for increasing electric fields. The cross-sectional area, A , of the drops is used to calculate the distribution of drop sizes. The size distributions for $d = 27, 55, 96$, and $202 \mu\text{m}$, each for a range of electric fields, are shown in Fig. 3. One can obtain an effective cross section radius $R = \sqrt{A/\pi}$ representing the radius of a circle with the same area as the roughly, but not completely, circular drops: this radius is depicted on the top axes of each graph. It should be noted that the initial average lateral size of the drops in all cases is much larger than the cell thickness: the initial drops are shaped like hockey pucks. Once the field exceeds a threshold, and the lateral extent of the drop is smaller than the thickness, the drops are more close to spherical.

The size distributions are obtained from image sequences of typically 1000 frames, obtained at different DC electric fields. At zero fields for all cell thicknesses there are only a few drops, with discrete peaks at high areas (corresponding to radii of $100 \mu\text{m}$ or greater) in each of the size distributions. These initial conditions (not shown in Fig. 3) are determined when the sample cell is filled. For non-zero fields, the image sequences are acquired once the system has reached a steady state. In order to obtain the lateral size of the droplet, the images must allow us to find the edge; this is, for example, not possible for fast-moving or fast-deforming drops. It is noteworthy to mention that the size distribution is obtainable up to higher fields for thinner cells: up to $12.5, 9.5$, and $2.5 \text{ V } \mu\text{m}^{-1}$ for cell thicknesses of $d = 55, 96$, and $202 \mu\text{m}$ respectively. For the thinnest ($d = 27 \mu\text{m}$) cell, the size distribution is measurable up to highest field probed, *i.e.* $18.5 \text{ V } \mu\text{m}^{-1}$.

First, we examine the thinnest two cells. Fig. 3(a) shows the drop size distribution for the first cell ($d = 27 \mu\text{m}$). For fields at and above $8.5 \text{ V } \mu\text{m}^{-1}$ (which is shown with red triangles), a shallow peak emerges at around $R_0 \sim 15 \mu\text{m}$: this corresponds to a diameter $2R$ that is roughly equal to the cell thickness d . For higher fields the peak shifts towards lower R and increases in magnitude. For the second cell ($d = 55 \mu\text{m}$, Fig. 3(b)), a peak at $R_0 \approx 20\text{--}25 \mu\text{m}$ emerges for $E \geq 6.5 \text{ V } \mu\text{m}^{-1}$ (shown with red triangles). This is, once again, consistent with $2R \sim d$. The magnitude of this peak, again, decreases for increasing fields with another peak emerging at lower radius. For both the first and second cells, the peak in the size distribution corresponding to a drop size that is comparable to the cell

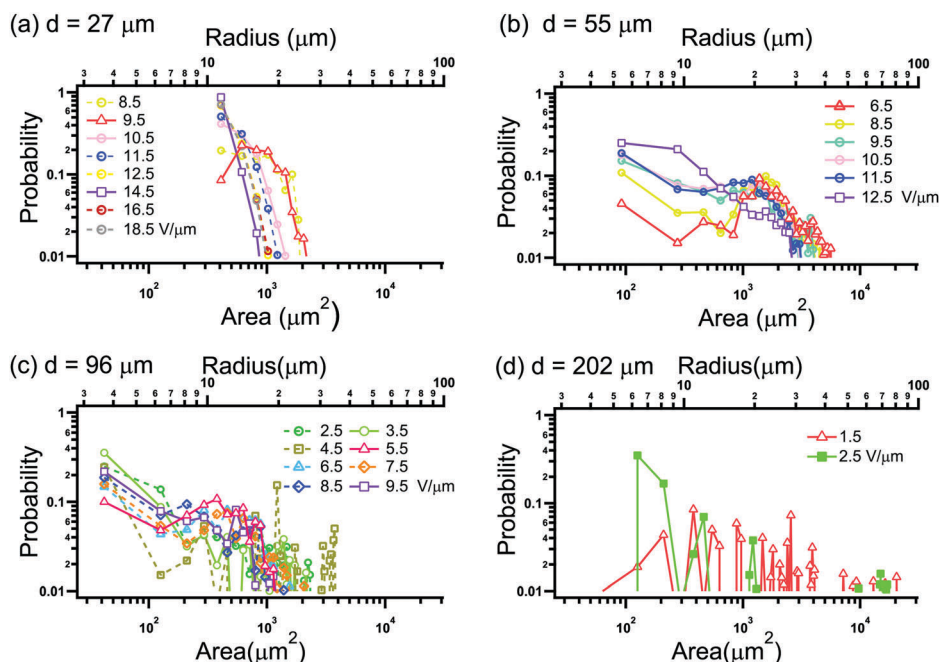


Fig. 3 Normalized drop size distribution obtained from 1000-image time series. The top axes shows the corresponding radius for different areas. (a) $d = 27 \mu\text{m}$: intermediate-field peak in the distribution at $R_0 \approx 10\text{--}20 \mu\text{m}$ shifts to $10 \mu\text{m}$ at highest fields. (b) $d = 55 \mu\text{m}$: intermediate-field peak at $R_0 \approx 20\text{--}25 \mu\text{m}$ shifts to lower R for higher fields. In both cases $2R_0/d \sim 1$. (c and d) $d = 96 \mu\text{m}$ and $d = 202 \mu\text{m}$: there is no peak at $2R/d = 1$, but merely a continuous shift of the size distribution to smaller R . Coalescence events are more common; this could be the cause of a small peak (in the $d = 96 \mu\text{m}$ cell) at $R \approx 10\text{--}20 \mu\text{m}$.

thickness likely arises from a stabilization of the drops by pinning at the top and bottom substrates. Eventually, however, at high enough fields, drops break up further and generate drops much smaller than the thickness of the cell. The smallest cross-sectional radius observed for these two sample thicknesses is around $10\ \mu\text{m}$.

Next, we examine the thicker cells. For the third cell, $d = 96\ \mu\text{m}$ (Fig. 3(b)), there is no clear peak at intermediate radii, but simply a continuous shift of the distribution towards lower radii as the field is increased, with a mean drop radius \bar{R} (shown in Fig. 4(a)) that is roughly between 10 and $20\ \mu\text{m}$ for all fields. Here, $2\bar{R} \ll d$. The fourth cell, $d = 202\ \mu\text{m}$ (Fig. 3(d)), is clearly in the bulk regime – the mean drop sizes (shown in Fig. 4(a)) are again much smaller than the cell thickness – and the static drop size distribution measurements are only possible for the lowest fields. Drop sizes are already strongly peaked at $R \sim 6\ \mu\text{m}$ for a (relatively) low field of $E = 2.5\ \text{V}\ \mu\text{m}^{-1}$. The statistics are poorer for the thickest cells, because the out-of-plane motion of the drops is increasingly important, and this makes it hard to get static droplet sizes from a single-plane image at fields. Notably, for both these cell thicknesses,

there is no peak at intermediate fields at $2R = d$. As well, for all samples at high field, the drop size distribution develops a peak for $R \leq 10\ \mu\text{m}$.

The mean drop radius, \bar{R} , versus electric field and for all thicknesses is shown in Fig. 4(a). Above the threshold, in the ranges $8.5\text{--}18.5\ \text{V}\ \mu\text{m}^{-1}$, $8.5\text{--}12.5\ \text{V}\ \mu\text{m}^{-1}$, $2.5\text{--}9.5\ \text{V}\ \mu\text{m}^{-1}$, and $1.5\text{--}2.5\ \text{V}\ \mu\text{m}^{-1}$ for $d = 27, 55, 96,$ and $202\ \mu\text{m}$, respectively, the radius decreases with increasing field. For all measurements made at high fields, \bar{R} approaches a value of between 10 and $20\ \mu\text{m}$.

We can now use the above information to get some insight into when the role of substrate becomes important. The importance of the electric stress relative to interfacial tension is measured by the electric capillary number, which for small drop deformations may be written as³⁰

$$\text{Ca}_E \equiv \frac{9|S^{-1}H - 1|M^{-1}}{10(H+2)^2(M^{-1}+1)} \frac{\varepsilon_0 k_{\text{in}} a E^2}{\gamma}. \quad (1)$$

In this system $S = \varepsilon_{\text{in}}/\varepsilon_{\text{ex}} = 0.67$, $H = \sigma_{\text{in}}/\sigma_{\text{ex}} = 0.10$, $M = \mu_{\text{in}}/\mu_{\text{ex}} = 0.17$, $\gamma \simeq 3\text{--}4\ \text{mN}\ \text{m}^{-1}$ is the interfacial tension between the oils, $\varepsilon_0 = 8.85 \times 10^{-12}\ \text{F}\ \text{m}^{-1}$ is the vacuum permittivity, $k_{\text{in}} = 2.4$ is the dielectric constant of drop, a is radius of the drop and E is the strength of the applied electric field. The electric capillary number is often defined simply as $\text{Ca}_E = \varepsilon_0 k_{\text{ex}} a E^2 / \gamma$. We follow instead Feng,³⁰ where one uses $\text{Ca}_E = \mu_{\text{ex}} U / \gamma$ with U being the maximum velocity at the drop surface calculated from the solution for a spherical drop. As the capillary number approaches unity one would expect the smooth liquid–liquid interface to become destabilized, and develop waves. In this system the electric capillary number can be written as $\text{Ca}_E = 0.9 \times 10^{-9} a E^2$ (where a and E are expressed in $\text{m}\ \text{k}\ \text{s}$ units). Fig. 4(b) shows the electric capillary number, for initial size of drops depending on the cell thickness, 130, 65, 95, and $60\ \mu\text{m}$ for $d = 27, 55, 96,$ and $202\ \mu\text{m}$, respectively, and at the critical electric field. The error bar symbol here denotes the extreme value if an average initial drop size of $85\ \mu\text{m}$ is used instead for all estimates. For cells of thickness above $\sim 100\ \mu\text{m}$, breakup occurs at $\text{Ca}_E \sim 0.3\text{--}1$ but increases as d decreases (the dotted line in Fig. 4(b) is a phenomenological fit to $1/d^\alpha$ with $\alpha = 1.5$). This is an indication that substrate interactions (which stabilize large droplets) are important for the lowest two cell thicknesses.

3.3 Drop motions: 2D motions in thin cells

The motion of drops, for $t < 0.8\ \text{s}$, is shown by a sequence of images for $d = 55\ \mu\text{m}$. Fig. 5(a) (upper panel) shows 4 frames with time interval of $0.2\ \text{s}$. One can see that the seven drops labelled in these frames deform and change shape slightly (as can be seen clearly from the edge of the drops (lower panel) found by the edge finding method. The velocity vectors indicating the direction of displacement are shown in Fig. 5(b).

The mean-squared displacements over the droplet centroids are shown in Fig. 6(a) and (b) for $d = 27$ and $d = 55\ \mu\text{m}$, respectively. One may write $\text{MSD} \sim t^\gamma$, where $\gamma < 1, = 1$ and > 1 represent sub-diffusive, diffusive, and super-diffusive motion.

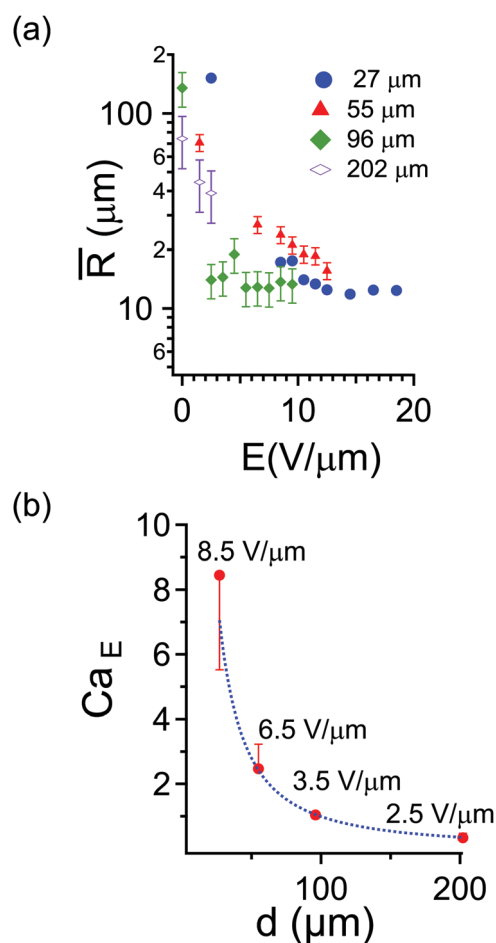


Fig. 4 (a) Mean drop radius \bar{R} as a function of electric field, for the samples of 4 cell thickness, d . (b) Capillary number versus cell thickness at the critical values of electric fields where drop breakup is observed. The electric capillary number Ca_E decreases as the cell thickness increases.

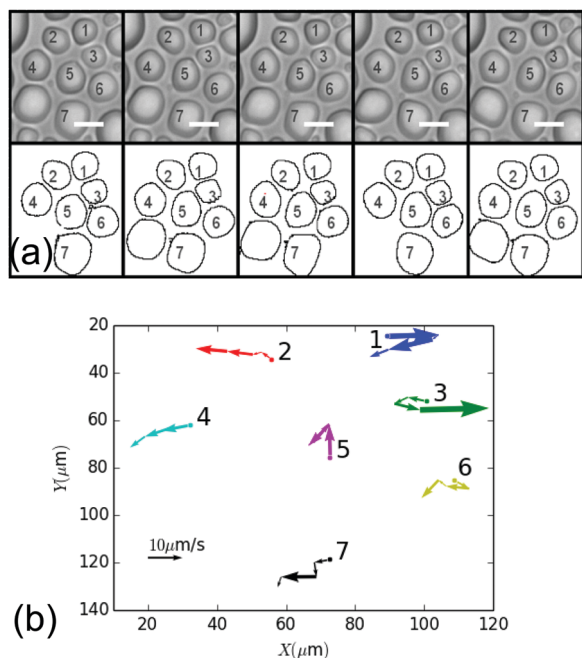


Fig. 5 (a) $d = 55 \mu\text{m}$. The deformation of drops (upper panel) tracked by edge detection (lower panel) for short times $t < 0.8 \text{ s}$ (from left to right, $\Delta t = 0, 0.2, 0.4, 0.6,$ and 0.8 s). Scale bar is $35 \mu\text{m}$. $E = 12.5 \text{ V } \mu\text{m}^{-1}$ (out of page). (b) Velocity vectors indicating direction of displacement of each labelled drops over 0.8 s . A small displacement of the particles between the frames is observed, with no clear directed motion.

For times $\log(t) < -0.5$, $\gamma \leq 1$ for both $d = 27 \mu\text{m}$ and $d = 55 \mu\text{m}$ cells. The errors in γ at short times are large; we therefore fit results for all fields to a single γ . For times $\log(t) > 0$, the

dynamics is clearly super-diffusive, with $\gamma \sim 1.4$, Fig. 6(c). Movie S2 (ESI[†]) displays the motion of drops over short times, $t = 1.0 \text{ s}$, and long times, $t = 10 \text{ s}$.

At higher electrohydrodynamic forcing, detecting droplet edges is challenging, but we can employ particle imaging velocimetry (PIV) to obtain the rms speeds, V_{rms} . The results of the PIV method are compared, for $d = 27 \mu\text{m}$, with the velocity of the fluid flow measured by particle tracking. For particle tracking, the function $\text{MSD} = K_1 t + K_2 t^2$ is used to fit the data. This is shown in ESI[†] (Fig. S1). Based on this function, $\sqrt{K_2}$ is the effective velocity magnitude of the fluid. Also, comparisons of the velocities, *via* PIV and particle tracking, are only possible when tracking is viable. For thin cells, $d = 27$ and $55 \mu\text{m}$, the velocity can be measured by tracking, but this method cannot be applied for the thicker cells, where PIV is the only feasible method.

Fig. 6(d) shows the measured velocities. A comparison between tracking and PIV for $d = 27 \mu\text{m}$ shows that the results from two methods are consistent in the low-field regime, where the flows are slow enough that droplet centroids move only a few pixels between successive time frames of image capture. The results are dramatic. While the maximum velocity observed for $d = 27 \mu\text{m}$ is $7 \mu\text{m s}^{-1}$, it is $300 \mu\text{m s}^{-1}$ for $d = 55 \mu\text{m}$, and there is a sharp threshold above $E = 12.5 \text{ V } \mu\text{m}^{-1}$, where this transition to strong electrohydrodynamic flow occurs. There is a clear link between the reduction of droplet sizes and the onset of super-diffusive motion. For example, in Fig. 4(a), for $d = 55 \mu\text{m}$, $2\bar{R}$ decreases to a value below the cell thickness d for $E = 6.5 \text{ V } \mu\text{m}^{-1}$ and greater. Fig. 6 shows that the motions for all fields ($E = 8.5 \text{ V } \mu\text{m}^{-1}$ and above) is super-diffusive.

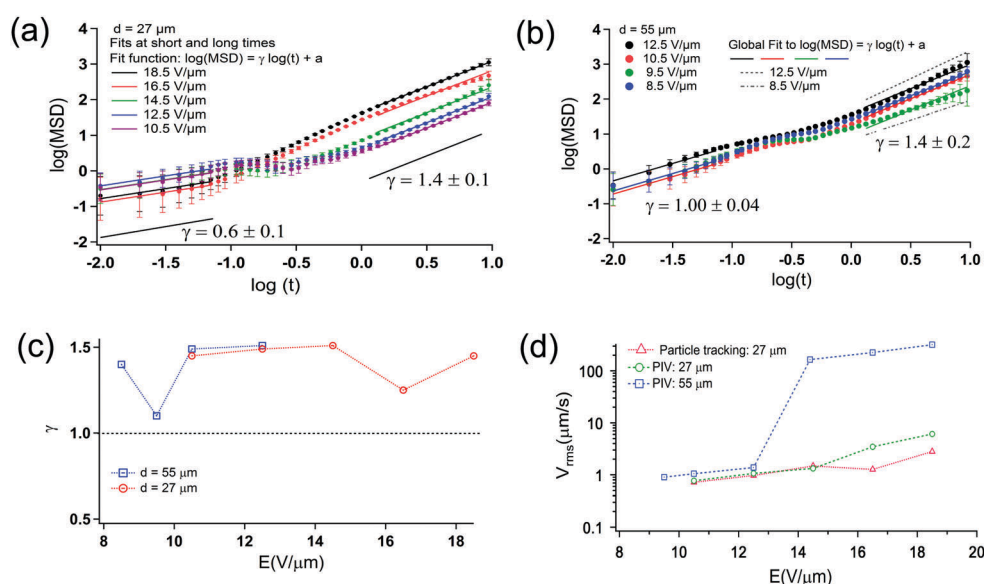


Fig. 6 Motions in thin cells. Mean-squared displacement vs. time obtained from particle tracking for (a) $d = 27 \mu\text{m}$ and (b) $d = 55 \mu\text{m}$. If one writes $\text{MSD} \sim t^\gamma$, a plot of $\log(\text{MSD})$ vs. $\log(t)$ shows a short-time regime ($\log(t) < -0.5$) where the dynamics appears either sub-diffusive or diffusive ($\gamma \leq 1$), and a long-time regime ($\log(t) > 0$) where the dynamics is clearly super-diffusive ($\gamma \sim 1.4$). (c) γ at long times and (d) V_{rms} using particle imaging velocimetry (PIV) as a function of electric field for the above two samples shows the remarkable, order-of-magnitude, increase in motions at high fields. For $d = 27 \mu\text{m}$, V_{rms} from PIV is compared with velocities obtained using particle tracking.

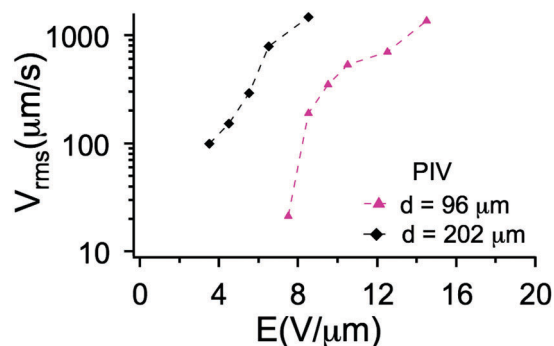


Fig. 7 Motions in thick cells. PIV analysis shows a sharp increase, by more than two orders of magnitude in V_{rms} from $10 \mu\text{m s}^{-1}$ to $1500 \mu\text{m s}^{-1}$ with increasing electric field. The threshold field for an increase above $300 \mu\text{m s}^{-1}$ is much smaller ($E = 5.5 \text{ V } \mu\text{m}^{-1}$) for the cell thickness $d = 202 \mu\text{m}$ than for $d = 96 \mu\text{m}$ ($E = 8.5 \text{ V } \mu\text{m}^{-1}$).

3.4 From 2D to quasi-3D motions

For thin cells, we saw three behaviours: first, a low-field regime where the mean-square droplet displacements are sub-diffusive or diffusive; second, an intermediate-field regime where the MSD is super-diffusive but still two-dimensional, and finally a high-field regime, where tracking is not possible, but PIV results show very large droplet velocities up to $300 \mu\text{m s}^{-1}$.

For the samples with cell thickness $d = 96$ and $202 \mu\text{m}$, we find that above a relatively low field threshold, the droplets exhibit visible out-of-plane motions. With increasing thickness, the maximum rms velocity observed is $7 \mu\text{m s}^{-1}$, $300 \mu\text{m s}^{-1}$, $1.4 \mu\text{m s}^{-1}$, and $1.6 \mu\text{m s}^{-1}$, respectively. Here the PIV analysis, based on only the X - Y components of displacements, are only indicative, and provided a lower bound on estimates of rms velocity, which is related to the droplet kinetic energy: $V_{\text{rms}} \propto \sqrt{E_{\text{kin}}}$. We find (Fig. 7) that there is a two orders-of-magnitude increase in the V_{rms} , corresponding to an order-of-magnitude increase in E_{kin} .

3.5 Onset of the regime of strong hydrodynamics

The regime of strong hydrodynamics is one where hydrodynamic forces dominate over dipolar forces. Much of the previous

analyses focus on the onset of droplet motions and do not address the out-of-plane motions seen in the movies for the thicker cells, which resemble the vertical overturning observed in Rayleigh–Bénard convection.³¹ Second, at high fields, very vigorous droplet motion that resembles a boiling liquid is observed. This is shown in Fig. 8(a) and (b) for $d = 55 \mu\text{m}$ (and $E = 18.5 \text{ V } \mu\text{m}^{-1}$) and for $d = 202 \mu\text{m}$ ($E = 8.5 \text{ V } \mu\text{m}^{-1}$), respectively.

To examine this phenomenon in a simpler system, we put fluorescent PMMA tracer particles in castor oil (with no silicone oil) to track the flows. This is challenging, because castor oil has a large Debye length, ($\kappa^{-1} \sim 1 \mu\text{m}$), and the tracer particles acquire a charge in a partially polar medium.³² Nevertheless, we can examine the phenomena at the threshold of particle motions. Shown in Fig. 9(a) is a snapshot of several convection cells for a cell with thickness of $54 \mu\text{m}$. Upon increasing the strength of the electric field from 0 to $2.4 \text{ V } \mu\text{m}^{-1}$ circulation patterns are observed inside the cell (see Movie S3, ESI†). An example of circulation patterns is shown in the time-lapse projection in Fig. 9(b). The arrows show the direction of circulations. The lengthscale of these circulations can be characterized by the lateral distance L between upward and downward flows (sources and sinks in a 2-dimensional time series). This lengthscale scales with the cell thickness d , with $2L/d \sim 1$ (see Fig. 9(c)). Typical “one-roll” structures in Rayleigh–Bénard convection (between rigid boundaries) are defined by a wavelength $\lambda_c = 2L \sim 2d$.³¹ What we observe appear to be two-roll structures, which have been reported in numerical studies of electrohydrodynamics.^{33,34} Thus, while the mechanism for the unsteady (and seemingly turbulent) motions is as yet unknown, the above observations suggest that the onset of unsteady motions is related to an electrical analog of Rayleigh–Bénard convection.

In the leaky dielectric picture, toroidal flows are the results of a liquid–liquid interface. The question arises, therefore, whether the flows observed for solid particles in castor oil are due to the presence of the particles (*i.e.* a kind of electro-osmotic flow). In a final experiment, the dye, Nile red, was mixed with castor oil. A cell was filled as follows: one end

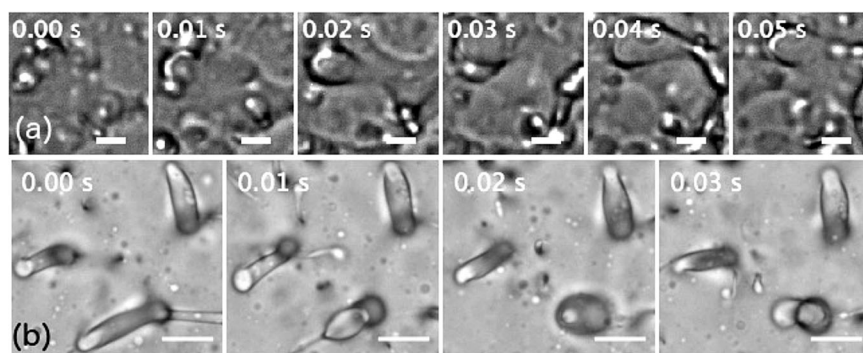


Fig. 8 (a) $d = 55 \mu\text{m}$, $E = 18.5 \text{ V } \mu\text{m}^{-1}$, perpendicular to the page. Time series shows 6 frames in 0.01 s intervals, displaying violent breakup, and coalescence of drops. Scale bar: $10 \mu\text{m}$. (b) $d = 202 \mu\text{m}$, $E = 8.5 \text{ V } \mu\text{m}^{-1}$, perpendicular to the page. Dynamics in the strong hydrodynamic regime results in “inversion”: local dynamical regions with cylindrical drops of castor oil inside a silicone oil background, which in turn is surrounded by castor oil. Scale bar: $50 \mu\text{m}$.

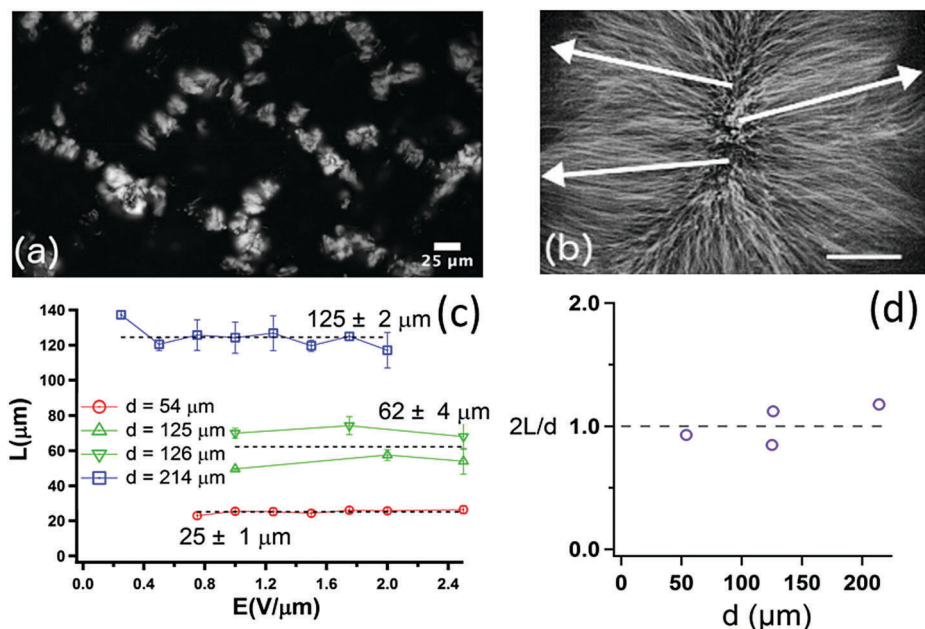


Fig. 9 Convective Instability in fluorescent PMMA colloids in castor oil. (a) Snapshot of several convection cells in a cell of thickness $d = 54 \mu\text{m}$. Scale bar: $25 \mu\text{m}$. (b) Convection rolls are observed for cells of different cell thickness d ; shown is a timelapse series (for the $d = 125 \mu\text{m}$ cell) that captures the flow of particles from a "source" in the centre (tail of the arrows) to a "sink" at the edge of the cell (head of the arrows). Scale bar: $25 \mu\text{m}$. (c) The characteristic length associated with the roll L scales with d . (d) The ratio $2L/d \sim 1$, which is consistent with a two-roll structure; see text.

containing the dyed castor oil and the other end containing the non-dyed castor oil, as shown in the panels of Fig. 10(a) and (b) which are obtained from a sequence of millimeter-scale photographs. In the first 3 hours, Fig. 10(a), the electric field was off

and the two regions are separable with a distinguishable boundary for all times. With the field on, $E = 8 \text{ V } \mu\text{m}^{-1}$ (pointing into the page), and in 16 minutes, Fig. 10(b), there is a blurring of the boundaries between the dyed and non-dyed regions (Movie S4, ESI[†]). Fig. 10(c) shows $(h - h_0)^2/2$, half the mean squared displacement of the interface between dyed and non-dyed regions *vs.* time; while h and h_0 are the position of the interface at time t and 0, respectively. An effective diffusion of coefficient can be calculated from $2D_{\text{eff}}^{E \neq 0} t = (h - h_0)^2$ which is $D_{\text{eff}}^{E \neq 0} = (0.31 \pm 0.01) \times 10^{-2} \mu\text{m}^2 \text{ s}^{-1}$. We could also measure the effective diffusion of dye molecules in the absence of the field, $D_{\text{eff}}^{E=0} \approx 0.56 \times 10^{-6} \mu\text{m}^2 \text{ s}^{-1}$, and compare it with the effective diffusion of mixing. There is clearly enhanced dynamics, $D_{\text{eff}}^{E \neq 0}/D_{\text{eff}}^{E=0} \approx 5500$, in the presence of the electric field. Since this enhanced motion occurs in the absence of either a second liquid or of solid tracer particles, neither the classic leaky-dielectric model for liquid-liquid interfaces nor electro-osmotic flows at the particle-fluid interface are relevant here. A possible mechanism is suggested by the work of Posner and Santiago,³⁵ which showed that electrokinetic flows can become unstable when conductivity gradients exist. While the ion concentration in the bulk of our samples is uniform, there are likely ionic gradients near the electrodes which give rise to the convective instability.

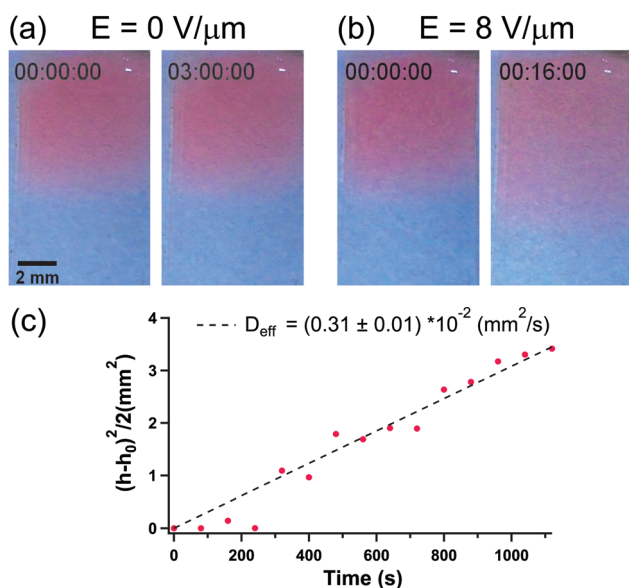


Fig. 10 Mixing of dyed and non-dyed castor oil in the presence of electric field: (a) $E = 0 \text{ V } \mu\text{m}^{-1}$ at $t = 0$ and $t = 3$ hours, no mixing of two regions was observed in the absence of field. (b) $E = 8 \text{ V } \mu\text{m}^{-1}$ (pointing into the page) at $t = 0$ and $t = 16$ minutes, enhanced mixing was observed in the presence of the field. (c) Half the mean squared displacement of the interface between dyed and non-dyed regions *vs.* time. The slope gives the effective diffusion coefficient of mixing at $E = 8 \text{ V } \mu\text{m}^{-1}$.

4 Conclusion

The collective behaviour of electrohydrodynamically driven dielectric oil droplets in a leaky dielectric medium is studied in this work as a function of the cell thickness. The effect of

sample thickness on droplet size distribution is studied first, followed by an examination of droplet dynamics, using two complementary methods: direct tracking of droplet centroids (particle tracking) as well as imaging velocimetry of the droplet interfaces (PIV).

The initial condition involves drops that have a lateral extent that is much larger than their thickness. The interactions of the drops with the substrate is therefore very important. For drop size and fields corresponding to $Ca_E \sim O(0.1)$, or smaller, droplets are not broken up further: this results in a peak in drop size distribution of $R \sim 10 \mu\text{m}$. For thin cells, $d = 27$ and $50 \mu\text{m}$, drop dynamics is practically two dimensional, and few coalescence events are observed.

The question of what is thick or thin can be addressed in two ways. First, the threshold field for drop breakup decreases with increasing the cell thickness, and for these fields the $Ca_E \gg 1$. Second, the threshold field, where particle tracking is feasible also decreases. A practical conclusion is that cells of thickness equal or larger than $100 \mu\text{m}$, while still much smaller than the lateral extent of a few centimeters, are thick enough for bulk behaviour to emerge.

For the thinnest cells, $d = 27$ and $d = 55 \mu\text{m}$, a transition from 2D random-walk-like motion with $\gamma \leq 1$ (likely driven by the stick-slip of the fluid–fluid–substrate contact line) to advective motion (characterized by $MSD \sim t^\gamma$ with $\gamma \sim 1.4$) is observed as a function of field. Droplet speeds of order $1 \mu\text{m s}^{-1}$ are seen for $d = 27 \mu\text{m}$, while speeds of order $100 \mu\text{m s}^{-1}$ are observed for $d = 27$ to $d = 55 \mu\text{m}$; at higher fields and higher cell thicknesses, one sees even more vigorous droplet motions $V_{\text{rms}} \sim 1000 \mu\text{m s}^{-1}$. For drop sizes $a > 10 \mu\text{m}$ (and given $\kappa^{-1} \sim 1 \mu\text{m}$), $\kappa a > 10$, the leaky dielectric model (valid for $\kappa a \gg 1$)¹⁴ is likely a reasonable description of the phenomena. However, in the strong hydrodynamic regime, where drop sizes $a < 10 \mu\text{m}$, κa is of order unity, and modeling the phenomena will also be more complicated.

For the thicker cells we additionally observe vertical overturning at remarkably low fields. The system is clearly more 3-dimensional and the pinning of the drops at the substrate is much less strong. Once again, at high fields, we see a transition to vigorous, unsteady flows. Analysis of these motions is more difficult because of the need to image the system in 3 dimensions; this will be the focus of future work. The overturning in thicker cells, prior to the onset of strong hydrodynamics, is reminiscent of Rayleigh–Bénard convection, and is also observed for PMMA colloidal particles in castor oil, where the convection rolls have a lateral scale that is proportional to the cell thickness. Counter to the expectation from the leaky dielectric model, we find that enhanced dynamics exists even in the absence of liquid–liquid interfaces, and also in the absence of solid–liquid interfaces. It is feasible that the origin of the convective flows is due to the presence of ionic gradients near the confining electrodes.

Recent efforts towards a more quantitative electrokinetic description^{14,21} of the electrohydrodynamic problem could provide a starting point for comparison with the phenomena described here. This work provides clear observations to look

for, as a function of cell thickness: the drop size distribution *versus* electric field (Fig. 3), the magnitude of the drop breakup threshold (Fig. 4), and the transition from slow motions to super-diffusive motions (Fig. 5–8). In addition, both the vertical overturning seen in emulsions as well as particle-laden fluid (Fig. 9 and Movie S3, ESI†) and the mixing of the carrier fluid in the presence of electric fields (Fig. 10 and Movie S4, ESI†) suggest the importance of a proper electrokinetic description.

Acknowledgements

Zena Aljabal is thanked for carrying out the impedance measurements. We thank Len Zedel for suggestions that led to this study, and Atul Varshney for useful discussions. This research was supported by National Science and Engineering Research Council of Canada (NSERC).

References

- 1 A. P. Gast and W. B. Russel, Simple ordering in complex fluids – Colloidal particles suspended in solution provide intriguing models for studying phase transitions, *Phys. Today*, 1998, **51**, 24–30.
- 2 W. Poon, Colloids as Big Atoms, *Science*, 2004, **304**(5672), 830–831.
- 3 A. Yethiraj, Tunable colloids: control of colloidal phase transitions with tunable interactions, *Soft Matter*, 2007, **3**, 1099–1115.
- 4 J. Dobnikar, A. Snezhko and A. Yethiraj, Emergent colloidal dynamics in electromagnetic fields, *Soft Matter*, 2013, **9**, 3693–3704.
- 5 D. A. Saville, Electrohydrodynamics: The Taylor–Melcher leaky dielectric model, *Annu. Rev. Fluid Mech.*, 1997, **29**, 27–64.
- 6 P. F. Salipante and P. M. Vlahovska, Electrohydrodynamics of drops in strong uniform dc electric fields, *Phys. Fluids*, 2010, **22**, 112110.
- 7 B. J. Kirby, *Micro- and nanoscale fluid mechanics: Transport in microfluidic devices*, Cambridge University Press, 2010.
- 8 M. Singh, H. M. Haverinen, P. Dhagat and G. E. Jabbour, Inkjet printing – Process and its application, *Adv. Mater.*, 2009, **22**, 673–685.
- 9 C. T. O’Konski and H. C. Thacher, The distortion of aerosol droplets by an electric field, *J. Phys. Chem.*, 1953, **57**, 955–958.
- 10 R. S. Allan and S. G. Mason, Particle behavior in shear and electric fields. I. Deformation and burst of fluid drops, *Proc. R. Soc. A*, 1962, **276**, 45–61.
- 11 G. I. Taylor, Studies in electrohydrodynamics I. The circulation produced in a drop by an electric field, *Proc. R. Soc. A*, 1966, **291**, 159–166.
- 12 J. R. Melcher and G. I. Taylor, Electrohydrodynamics: A review of the role of interfacial shear stresses, *Annu. Rev. Fluid Mech.*, 1969, **1**, 111–146.
- 13 S. Torza, R. G. Cox and S. G. Mason, Electrohydrodynamic deformation and burst of liquid drops, *Philos. Trans. R. Soc., A*, 1971, **269**, 295–321.

- 14 E. K. Zholkovskij, J. H. Masliyah and J. Czarnecki, An electrokinetic model of drop deformation in electric field, *J. Fluid Mech.*, 2002, **427**, 1–27.
- 15 J. A. Lanauze, L. M. Walker and A. S. Khair, Nonlinear electrohydrodynamics of slightly deformed oblate drops, *J. Fluid Mech.*, 2015, **774**, 245–266.
- 16 A. Varshney, S. Ghosh, S. Bhattacharya and A. Yethiraj, Self organization of exotic oil-in-oil phases driven by tunable electrohydrodynamics, *Sci. Rep.*, 2012, **2**, 1–6.
- 17 A. Varshney, S. Gohil, M. Sathe, R. V. Seshagiri Rao, J. B. Joshi, S. Bhattacharya, A. Yethiraj and S. Ghosh, Multiscale flow in an electro-hydrodynamically driven oil-in-oil emulsion, *Soft Matter*, 2016, **12**, 1759–1764.
- 18 A. Groisman and V. Steinberg, Elastic turbulence in a polymer solution flow, *Nature*, 2000, **27**, 53–55.
- 19 J. D. Posner, C. L. Perez and J. G. Santiago, Electric fields yield chaos in microflows, *Proc. Natl. Acad. Sci. U. S. A.*, 2012, **109**, 14353–14356.
- 20 J. C. Baygents and D. A. Saville, Electrophoresis of drops and bubbles, *J. Chem. Soc., Faraday Trans.*, 1991, **12**, 1883–1898.
- 21 O. Schnitzer and E. Yariv, The Taylor Melcher leaky dielectric model as a macroscale electrokinetic description, *J. Fluid Mech.*, 2015, **773**, 1–33.
- 22 J. Crocker and D. Grier, Methods of digital video microscopy for colloidal studied, *J. Colloid Interface Sci.*, 1996, 179.
- 23 A. Fincham and G. Spedding, Low cost, high resolution dpiv for measurement of turbulent fluid flow, *Exp. Fluids*, 1997, **23**, 449–462.
- 24 A. Fincham and G. Delerce, Advanced optimization of correlation imaging velocimetry algorithms, *Exp. Fluids*, 2000, **29**, 13–22.
- 25 J. Petit, D. Rivire, H. Kellay and J.-P. Delville, Break-up dynamics of fluctuating liquid threads, *Proc. Natl. Acad. Sci. U. S. A.*, 2012, **109**, 18327–18331.
- 26 J. D. Sherwood, Breakup of fluid droplets in electric and magnetic fields, *J. Fluid Mech.*, 1988, **188**, 133–146.
- 27 R. Pillai, J. D. Berry, D. J. E. Harvie and M. R. Davidson, Electrokinetics of isolated electrified drops, *Soft Matter*, 2016, **12**, 3310–3325.
- 28 R. B. Karyappa, S. D. Deshmukh and R. M. Thaokar, Breakup of a conducting drop in a uniform electric field, *J. Fluid Mech.*, 2014, **754**, 550–589.
- 29 H. Nganguia, Y. N. Young, A. T. Layton, M. C. Lai and W. F. Hu, Electrohydrodynamics of a viscous drop with inertia, *Phys. Rev. E*, 2016, **93**, 1–9.
- 30 J. Q. Feng, Electrohydrodynamic Behaviour of a Drop Subjected to a Steady Uniform Electric Field at Finite Electric Reynolds Number, *Proc. R. Soc. A*, 1999, **455**, 2245–2269.
- 31 A. V. Getling, *Rayleigh – Benard convection: Structures and dynamics*, World Scientific, 1998.
- 32 A. Yethiraj and A. van Blaaderen, A colloidal model system with an interaction tunable from hard sphere to soft and dipolar, *Nature*, 2003, **4210**, 513–517.
- 33 P. A. Vázquez, G. E. Georghiou and A. Castellanos, Numerical analysis of the stability of the electrohydrodynamic (EHD) electroconvection between two plates, *J. Phys. D: Appl. Phys.*, 2008, **41**, 175303.
- 34 A. Kourmatzis and J. S. Shrimpton, Characteristics of electrohydrodynamic roll structures in laminar planar Couette flow, *J. Phys. D: Appl. Phys.*, 2016, **49**, 045503.
- 35 J. D. Posner and J. G. Santiago, Convective instability of electrokinetic flows in a cross-shaped microchannel, *J. Fluid Mech.*, 2006, **555**, 1–42.